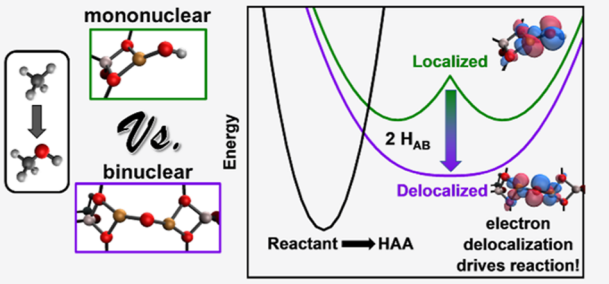
Methane Activation by a Mononuclear Copper Active Site in the Zeolite Mordenite: Effect of Metal Nuclearity on Reactivity

Alexander J. Heyer,[‖] Dieter Plessers,[‖] Augustin Braun, Hannah M. Rhoda, Max L. Bols, Britt Hedman, Keith O. Hodgson, Robert A. Schoonheydt,* Bert F. Sels,* and Edward I. Solomon*

ABSTRACT: The direct conversion of methane to methanol would have a wide reaching environmental and industrial impact. Copper-containing zeolites can perform this reaction at low temperatures and pressures at a previously defined O_2-activated $[Cu_2O]^{2+}$ site. However, after autoreduction of the copper-containing zeolite mordenite and removal of the $[Cu_2O]^{2+}$ active site, the zeolite is still methane reactive. In this study, we use diffuse reflectance UV−vis spectroscopy, magnetic circular dichroism, resonance Raman spectroscopy, electron paramagnetic resonance, and X-ray absorption spectroscopy to unambiguously define a mononuclear $[CuOH]^+$ as the CH_4 reactive active site of the autoreduced zeolite. The rigorous identification of a mononuclear active site allows a reactivity comparison to the previously defined $[Cu_2O]^{2+}$ active site. We perform kinetic experiments to compare the reactivity of the $[CuOH]^+$ and $[Cu_2O]^{2+}$ sites and find that the binuclear site is significantly more reactive. From the analysis of density functional theory calculations, we elucidate that this increased reactivity is a direct result of stabilization of the $[Cu_2OH]^{2+}$ H-atom abstraction product by electron delocalization over the two Cu cations via the bridging ligand. This significant increase in reactivity from electron delocalization over a binuclear active site provides new insights for the design of highly reactive oxidative catalysts.



1. INTRODUCTION

The direct conversion of methane to methanol is a reaction of paramount importance with both environmental and industrial interest. Given the strong C−H bond of methane (104 kcal/mol) and the tendency for overoxidation of the methanol product, the main route of selective methane oxidation utilizes a harsh and expensive process involving a syngas intermediate.[1] This precludes employing this syngas route at small-scale oil extraction sites, leading to wasteful methane flaring and unnecessary greenhouse gas production. However, nature has solved this problem. The enzymes soluble and particulate methane monooxygenase (sMMO and pMMO) use iron and copper cofactors, respectively, to transform methane into methanol under ambient conditions. The iron active site in sMMO is a clearly defined binuclear site, while the nature of the copper active site in pMMO is an open question with proposals for a mononuclear, binuclear, or trinuclear active site.[2−8] Similar to the enzymes, iron and copper exchanged zeolites can also selectively convert methane to methanol under relatively mild conditions, employing many of the characteristics that make their enzyme analogues so reactive but in a material that can be potentially scaled for industrial use.[9−11]

Copper zeolites are prepared for methane reaction by first performing an aqueous exchange with a cupric salt and calcining the resulting material (heating in O_2 at 450 °C), combusting the anionic portion of the Cu salt and dehydrating the zeolite. This calcined material can selectively convert methane to methanol. However, this Cu(II) active site can be reduced by heating in helium at high temperatures (≥500 °C) concurrent with the release of O_2 in a process called autoreduction. The reduced active site can be reactivated for methane oxidation by the addition of N_2O or O_2. We rigorously defined this active site as a $[Cu_2O]^{2+}$ species.[12−14] Recently, there have been reports that the autoreduced zeolite of the topology mordenite (MOR), which should have its $[Cu_2O]^{2+}$ active site reduced, is still able to oxidize methane to methanol. Whether or not this is due to a different active site or whether the autoreduced zeolite has been partially activated

by O_2 leaks creating $[Cu_2O]^{2+}$ sites has been an open issue.[15,16]

In this study, we investigate the CH_4 reaction of the autoreduced MOR zeolite using electron paramagnetic resonance (EPR), X-ray absorption spectroscopy (XAS), diffuse reflectance UV−vis (DR UV−vis) spectroscopy, magnetic circular dichroism (MCD), and resonance Raman (rR) spectroscopy. We define the active site of the autoreduced zeolite as a mononuclear $[CuOH]^+$ bound bidentate to an aluminate tetrahedral site (T-site). Although this active site has been proposed in past studies,[17−19] it has not been rigorously experimentally demonstrated with multiple spectroscopies nor associated with the autoreduced zeolite.

Having a well-defined mononuclear active site allows comparison to the previously defined binuclear $[Cu_2O]^{2+}$ active site to assess the effects of metal nuclearity on reactivity. This is important given that the reactivity of the $[CuOH]^+$ site is an open question with claims of it being a non-reactive precursor site[20] to claims that it has a lower activation barrier for reaction with CH_4 than the binuclear $[Cu_2O]^{2+}$ active site.[19] We find experimentally that the $[CuOH]^+$ site has a significantly higher barrier ($\Delta H^{\ddagger}$ = 15.7 kcal/mol) than the $[Cu_2O]^{2+}$ active site ($\Delta H^{\ddagger}$ = 6.2 kcal/mol) for H-atom abstraction (HAA) from CH_4. Using density functional theory (DFT) calculations, we compare models for $[CuOH]^+$ and $[Cu_2O]^{2+}$ and elucidate that the weak ligand field and the low-coordination environment of the zeolite lattice activate both the mononuclear and binuclear Cu sites to perform methane activation with similar intrinsic barriers. However, the binuclear site is much more reactive in HAA due to its ability to stabilize the $[Cu_2OH]^{2+}$ product of HAA by electron delocalization over the two Cu ions via a superexchange interaction through the bridging oxo ligand. The increased binuclear driving force due to delocalization indicates the importance of metal nuclearity for low-temperature reactivity. Such information can greatly aid in designing better oxidation catalysts generally and in providing insights into the role that the higher nuclearity models of pMMO can play in enhancing C−H bond cleavage by delocalization of the electron gained from HAA.[4−8]

2. RESULTS AND ANALYSIS

2.1. Physical Properties. Autoreduced Cu-MOR samples were prepared in three steps: aqueous exchange with Cu(II) acetate on the parent Na-MOR zeolite, calcination with O_2 at 450 °C to burn off acetate and dehydrate, and heating in helium at 500 °C overnight to generate the autoreduced form (see Section S1). The Cu/Al ratio was determined to be 0.45 from inductively coupled plasma atomic emission spectroscopy (Table S1). These steps do not perturb the inherent structure of the zeolite lattice, and no large copper oxide clusters were detected by powder X-ray diffraction (PXRD) (Figure S1). The microporosity was determined to be similar for Na-MOR and Cu-MOR (0.18 cm^3/g) by N_2 physisorption, in agreement with literature values (Figure S2).[21]

2.2. Characterization and CH_4 Reaction of Autoreduced Cu-MOR. Autoreduced Cu-MOR has two distinct EPR active S = 1/2 Cu(II) sites (Figure 1A black). These two axial species have the following EPR parameters:[22,23] $g_{\|}$ = 2.27, $A_{\|}$ = 191 × 10^{-4} cm^{-1}, $g_{\perp}$ = 2.09, and $A_{\perp}$ = 18−42 × 10^{-4} cm^{-1}, referred to as MOR-A, and $g_{\|}$ = 2.32, $A_{\|}$ = 169 × 10^{-4} cm^{-1}, $g_{\perp}$ = 2.07, and $A_{\perp}$ = 9−22 × 10^{-4} cm^{-1}, referred to as MOR-B (with sharp $g_{\perp}$ hyperfine features observed in other studies).[24]

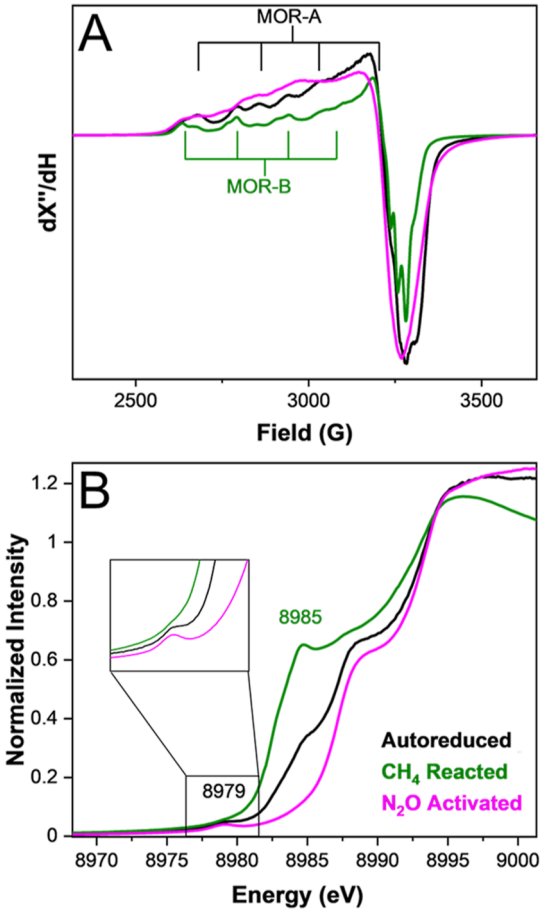


Figure 1. EPR (A) and XAS (B) spectra of autoreduced (black), CH_4-reacted (green), and N_2O-activated (pink) Cu-MOR.

These two sites account for 55 ± 11% of the total copper based on spin quantification. Reaction of the autoreduced zeolite with CH_4 at 200 °C selectively reduces MOR-A, lowering the amount of EPR active copper in the zeolite from 55 ± 11% to 25 ± 5% (Figure 1A green). This occurs concurrent with the production of methanol obtained through aqueous or steam extraction of the CH_4-reacted sample. Thus, MOR-A and MOR-B account for 30 ± 12% and 25 ± 5%, respectively, of the total copper present in the autoreduced Cu-MOR. The remaining copper is not EPR detectable (down to 5 K and a field region of 0-4000 G).

XAS provides a complimentary technique to analyze the ratio of total Cu(I)/Cu(II) in the sample using the pre-edge and the rising edges (the extended fine structure region did not provide useful information due to heterogeneity, as presented in Explanation S1). XAS of autoreduced MOR reveals overlapping features in the 8983−8985 eV region associated with the 1s → 4p transition of the Cu(I) in the sample along with an 8979 eV peak that is the 1s → 3d transition of the Cu(II) present (Figure 1B black).[25] Reaction of the autoreduced Cu-MOR sample with N_2O results in total oxidation as there is no remaining Cu(I) feature in the XAS spectrum from 8983 to 8985 eV (2.5 ± 2.5% Cu(I)) (Figure 1B pink and Explanation S2). This N_2O reaction of autoreduced Cu-MOR also results in the appearance of a 22 000 cm^{-1} charge transfer (CT) band in the DR UV−vis spectrum (Figure S3) that corresponds to the previously assigned $[Cu_2O]^{2+}$ active sites.[13] The bicuprous precursors of

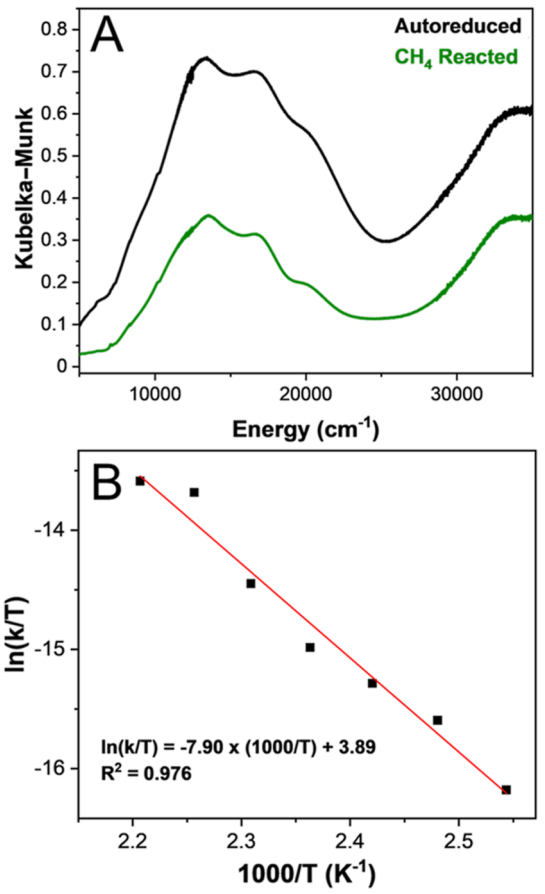


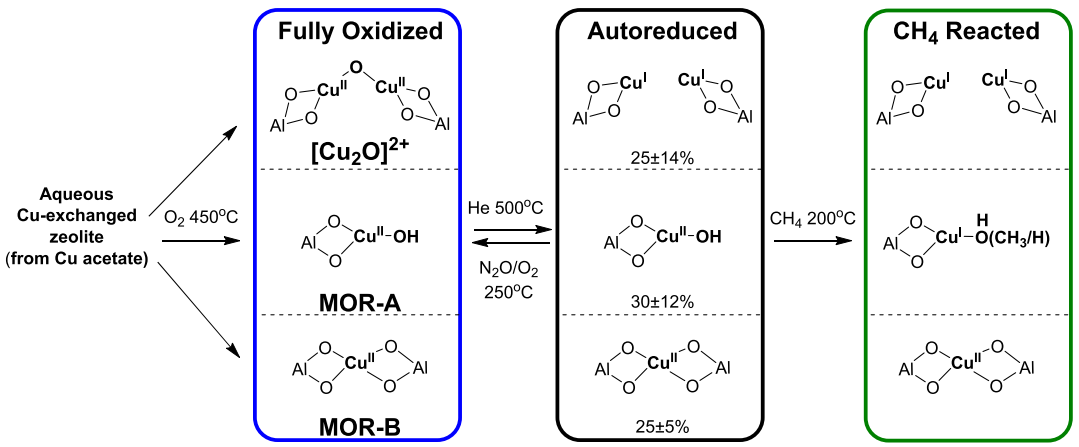
Figure 2. (A) DR UV−vis spectra of autoreduced (black) and CH_4-reacted (green) Cu-MOR. (B) Eyring plot of the loss of the DR UV−vis signal from 20 000 to 22 000 cm^{-1} for the reaction of autoreduced Cu-MOR with CH_4.

these $[Cu_2O]^{2+}$ active sites in autoreduced Cu-MOR quantify to 25 ± 14% total copper (Explanation S2). This $[Cu_2O]^{2+}$ species is absent in the autoreduced Cu-MOR, as evidenced by the lack of the characteristic 22 000 cm^{-1} CT band in the DR UV−vis spectrum (Figure 2A) and the lack of characteristic vibrations in the rR spectrum with excitation at 458 nm (vide infra). From a combination of the above EPR and XAS results, we estimate that the autoreduced Cu-MOR has 30 ± 12% MOR-A, 25 ± 5% MOR-B, and 25 ± 14% bicuprous sites that are precursors to $[Cu_2O]^{2+}$ active sites. Given the measurement errors [in particular the Cu(I) estimate from XAS] there is the open possibility of up to 20 ± 19% unaccounted for copper either from the error in Cu(I) quantification or from Cu(II) that is EPR silent due to magnetic coupling but PXRD silent due to the small cluster size.

In parallel with the loss of the MOR-A EPR signal (with the production of CH_3OH), reaction of the autoreduced zeolite with CH_4 results in an increase in intensity in the 8983−8985 eV region of the XAS spectrum and a loss of intensity in the pre-edge at 8979 eV, both consistent with Cu(II) reduction (Figure 1B green). Given the single turnover conditions, the additional Cu(I) upon CH_4 reduction directly relates to the active site quantity. The CH_4 reacted sample shows a 45 ± 20% increase in Cu(I) XAS intensity relative to the autoreduced sample (Explanation S2), within the error of the 30 ± 12% loss of the MOR-A site observed in EPR. Although the error in these quantifications leaves open the possibility of other methane reactive sites, the loss of the MOR-A signal is sufficient to explain the reduction observed in XAS. Thus, we can directly correlate the loss of EPR signal intensity to active site reactivity and assign MOR-A as the CH_4 reactive site in autoreduced Cu-MOR. This reaction produces 0.1 mol methanol/mol total Cu (Table S1), equivalent to 0.33 ± 0.14 mol methanol/mol MOR-A [Note that two mononuclear Cu(II) sites are required for producing one mol of methanol, vide infra]. After the extraction of methanol, the addition of oxygen and dehydration by heating in helium to 500 °C allows regeneration of the autoreduced zeolite (Figures S4 and S5) that can subsequently react with CH_4 to form the same amount of methanol.

Using this information, we can model the evolution of copper species in the zeolite under various conditions (Scheme 1). After aqueous exchange of copper acetate into the zeolite, calcination removes acetate ions and dehydrates the zeolite to leave copper ions bound to the lattice. This results in the $[Cu_2O]^{2+}$ site assigned in our previous study[13] and MOR-A and MOR-B analyzed here. The identity of the MOR-A site will be discussed in Sections 2.3 and 2.4. The MOR-B site is thought to be ligated by two aluminum sites,[23] lowering its oxidizing potential and making it unreactive with CH_4, as revealed in this study (Figure 1A). The $[Cu_2O]^{2+}$ sites can be selectively reduced by heating in helium to result in the autoreduced material, which is the focus of this study. The

Scheme 1. Composition of Species in Cu-MOR under Various Conditions



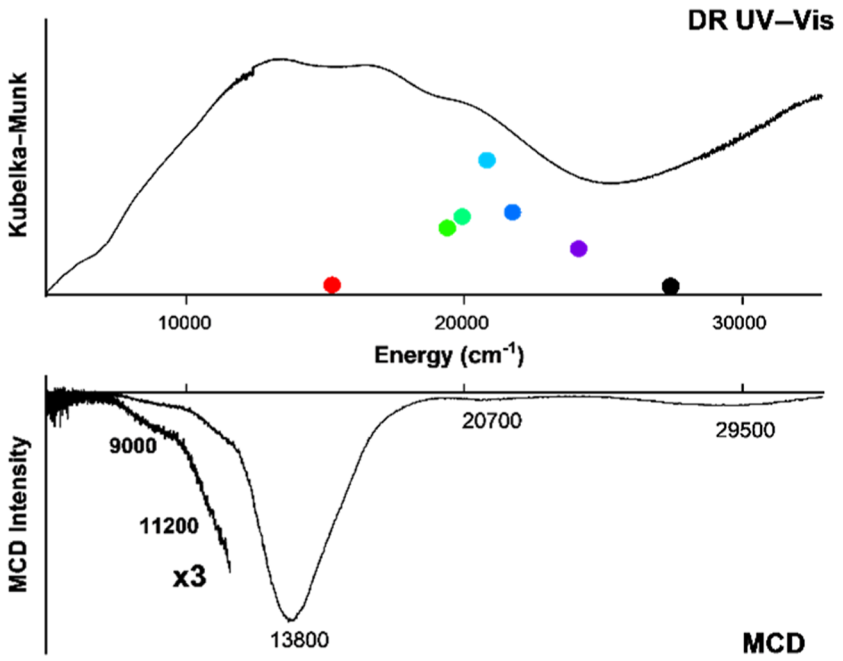


Figure 3. DR UV–vis (top) and MCD (bottom) spectra of autoreduced Cu-MOR. ●—Dots correspond to the equally colored rR spectra of Figure S11, measured at different laser energies corresponding to the location of the dot on the *x*-axis. The relative intensities of the rR spectra (normalized to the lattice vibration at 480 cm^{-1}) correspond to the height of the dot in the figure. This gives the rR excitation profile.

$[Cu_2O]^{2+}$ site can be regenerated through oxidation in O_2 or N_2O. Through EPR, XAS, DR UV–vis spectroscopy, and rR spectroscopy (vide infra), we demonstrate that in the autoreduced sample, only the MOR-A site reacts with CH_4 and is selectively reduced in this reaction. The MOR-A Cu(II) active site's ability to break the strong C–H bond of CH_4 motivates our investigation into its geometric and electronic structure explored below.

2.3. Spectroscopic Definition of the MOR-A Active Site. To gain more insights into the nature of the MOR-A site, DR UV–vis spectra of the autoreduced and CH_4 reacted samples were collected (the spectrum of dried Na-MOR was collected as a comparison in Figure S6). Autoreduced Cu-MOR has overlapping features, which lose intensity across the spectral envelope upon the reaction with CH_4 (Figure 2A). The broadness of the features makes them difficult to parse for chemical information. There is also the issue of contributions from multiple species simultaneously, for example., MOR-A and MOR-B. MCD is an optical technique that provides complementary information on electronic transitions to DR UV–vis spectroscopy.[26] While the DR UV–vis spectrum has electronic transitions from all species in the zeolite, the MCD spectrum of autoreduced Cu-MOR reveals transitions that are all C-terms (temperature- and field-dependent transitions), indicating they are specifically the electronic transitions of the paramagnetic MOR-A and MOR-B sites rather than Cu(I) or potential EPR silent Cu(II) in the sample (Figures S7 & S8). The MCD spectrum of autoreduced Cu-MOR reveals low-energy, low-intensity excited states at 9000 and 11 200 cm^{-1}, intense overlapping features above 10 000 cm^{-1} with a maximum at 13 800 cm^{-1}, and two higher energy features with low MCD intensity at 20 700 and 29 500 cm^{-1} (Figure 3). The CH_4-reacted Cu-MOR MCD spectrum (with no MOR-A EPR signal) has a positive feature around 9000 cm^{-1} and no feature at 21 000 cm^{-1}, indicating that the MOR-A site has a negative feature at 9,000 cm^{-1}, overlapping negative features around 13 500 cm^{-1}, and a weak negative feature at 21 000 cm^{-1} (Figure S9). MCD C-term intensity originates from spin–orbit coupling (SOC) (large for metal-centered transitions), whereas DR UV–vis intensity reflects the electric dipole moment of the transition. Thus, metal-centered d–d transitions (that are electric dipole forbidden but with high SOC) have large MCD/diffuse reflectance intensity ratios relative to ligand to metal CT bands (that are electric dipole allowed but with low SOC). Consequently, we can use the combination of DR UV–vis spectroscopy and MCD to assign MOR-A's low energy features centered at 13 500 cm^{-1} as multiple Cu d–d transitions (large MCD to diffuse reflectance intensity ratios) and its higher energy features at 20 700 and 29 500 cm^{-1} as CT bands (small MCD to diffuse reflectance intensity ratios).

The assignment of MOR-A's CT bands using MCD and DR UV–vis spectroscopy provides an opportunity to obtain vibrational information on the active site using rR spectroscopy. Laser excitation of autoreduced Cu-MOR at 458 nm enhances three vibrational features at 552, 750, and 981 cm^{-1} that are lost upon reaction with CH_4 (Figure 4A black vs green). There are also no clear resonance-enhanced $[Cu_2O]^{2+}$ vibrations (very intense in the rR spectrum at 460 and 530 cm^{-1}) nor any vibrations at energies above 1000 cm^{-1} (Figure S10). We thus see no evidence of $[Cu_2O]^{2+}$ active sites in autoreduced Cu-MOR. The vibrations we do observe profile with the 20 700 cm^{-1} MOR-A CT band, associating these vibrations with the MOR-A active site (Figure 3 top and Figure S11).

To gain further information on the vibrations, ^{18}O and D isotope labels were incorporated into the active site by repeatedly steaming the autoreduced zeolite at 200 °C with $H_2{}^{18}O$ or D_2O and subsequently drying the zeolite in He at 500 °C. This procedure reproduces the DR UV–vis and EPR spectra of the autoreduced zeolite (Figures S12 and S13) and maintains the integrity of the active site while incorporating an

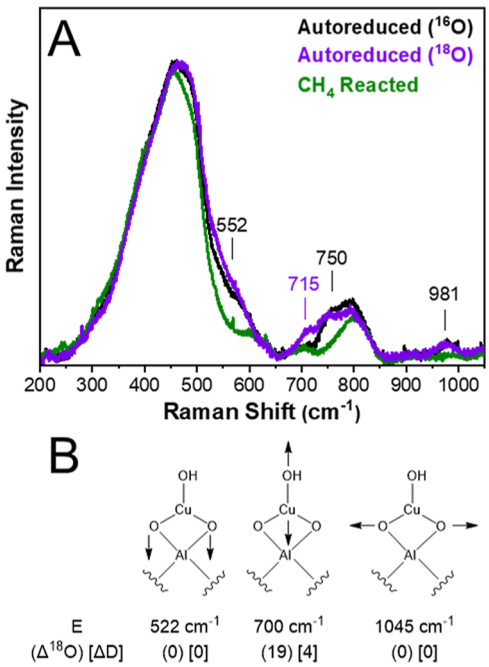


Figure 4. (A) rR spectrum of autoreduced (black), ^{18}O-labeled autoreduced (purple), and CH_4-reacted (green) Cu-MOR. λ_{ex} = 458 nm. (B) DFT-predicted rR vibrations and isotope shifts of the T1 Site 2 model of $[CuOH]^+$.

isotope label. Water has been used in past studies to incorporate isotope labels into the zeolite through isotope scrambling after hydration.[27] Although there are no observable isotope shifts in the 552 and 981 cm^{-1} MOR-A rR features of the $H_2{}^{18}O$-treated sample, there is a red shift of the 750 cm^{-1} feature by 35 cm^{-1}, indicating that an exchangeable oxygen is associated with this vibration (Figure 4A purple). Treating the 750 cm^{-1} vibration as a harmonic oscillator Cu−O stretch where the O belongs to an extra lattice ligand predicts a red shift to 716 cm^{-1}, as observed. This 750 cm^{-1} vibration indicates a strong Cu−O bond corresponding to a short 1.71 Å bond length from Badger's rule.[28] Steaming and heating with D_2O does not detectably perturb any features (Figure S14). This is expected as 5 cm^{-1} is the smallest isotope shift that would be detectable on the 750 cm^{-1} feature based on the instrument resolution and the broadness of the feature, and a 4 cm^{-1} red shift is predicted based on our $[CuOH]^+$ active site model vide infra.

The S = 1/2 EPR signal and the strong Cu−O stretch vibration provide handles to define the MOR-A site. The binuclear $[Cu_2O]^{2+}$ site first identified by Woertink et al. is an oxo-bridged binuclear Cu(II) site. Thus, the overall spin must either be S = 1 or S = 0, and a $[Cu_2O]^{2+}$ site is excluded for MOR-A.[12] A binuclear site that could match the S = 1/2 MOR-A spin would be a localized mixed valent Cu(I)Cu(II) site. This possibility was eliminated by N_2O oxidation of essentially all Cu(I) (Figure 1B) with no change in the MOR-A EPR signal (Figure 1A). Trinuclear Cu(II) centers have been proposed to exist in Cu-MOR[29] and are S = 1/2; however, they exhibit a large derivative-shaped pseudo-A term in MCD that is not observed for MOR-A (Figure 3).[30] This limits MOR-A to a mononuclear Cu(II) site. Among the mononuclear site possibilities, an end-on superoxo and a Cu(II) oxyl can be excluded because they would have triplet ground states.[31,32] An end-on hydroxoperoxo would match the spin, but its rR spectrum would exhibit a Cu−O stretch at a lower energy (~624 cm^{-1}) and a higher intensity, isotope-sensitive O−O stretch at >800 cm^{-1} that is not present in the observed rR spectrum (Figure 4A).[33] The remaining possibility is a mononuclear cupric hydroxide. This matches the spin, and a DFT model for the site matches the DR UV−vis, MCD, and rR experimental data well (vide infra). We thus assign MOR-A as a $[CuOH]^+$ bound to the zeolite lattice. This site has clear spectroscopic handles that allow its assignment in other lattices, including in the autoreduced copper-containing MFI topology (Figures S15−17), indicating that it is not unique to the MOR topology.

Thus, the CH_4 oxidation active site in autoreduced Cu-MOR is a $[CuOH]^+$ species that is not reduced upon autoreduction, distinctly different from the $[Cu_2O]^{2+}$ active site that is lost upon heating in helium. A $[CuOH]^+$ methane reactive active site has been proposed in the literature,[17−19] but here, we provide the first rigorous definition of this active site as well as its association with methanol production by autoreduced zeolites. The reactivity of this $[CuOH]^+$ site also lacks consensus in the literature with reports that it is a non-reactive precursor site[20] and reports that it is has a lower barrier than the highly reactive $[Cu_2O]^{2+}$ site.[19] The reactivity of this spectroscopically well-defined $[CuOH]^+$ active site with CH_4 can now be compared to the $[Cu_2O]^{2+}$ active site defined earlier. We chose to compare this to the $[Cu_2O]^{2+}$ in the CHA topology. This model was experimentally validated by comparing the CuOCu angle of multiple generated $[Cu_2O]^{2+}$ structures to the CuOCu angle determined by normal coordinate analysis of the rR vibrations.[14] We chose this model to compare to the $[CuOH]^+$ site in MOR given its existing detailed computational analysis of its reactivity[14] and the fact that it contains only a single $[Cu_2O]^{2+}$ site in contrast to the multiple $[Cu_2O]^{2+}$ sites present in Cu-MOR.[13]

Woertink et al. observed a CH_4/CD_4 kinetic isotope effect in Cu-MFI, indicating that the rate-limiting step in the reaction of the $[Cu_2O]^{2+}$ site with CH_4 in Cu-MFI is the C−H bond cleavage by the copper active site.[12] Thus, CH_4 transport is faster than C−H bond cleavage by the $[Cu_2O]^{2+}$ in MFI. This can be reasonably assumed for the $[CuOH]^+$ in MOR as it has larger channels, making CH_4 transport more facile, and yet a slower reaction is observed (vide infra). This indicates that the rate must be related to the reactivity of the Cu active site. Autoreduced Cu-MOR was reacted with CH_4, and the decay of the MOR-A 21 000 cm^{-1} CT band was monitored using DR UV−vis spectroscopy to extract a first-order rate constant (Figure S18). This was repeated for multiple temperatures to generate an Eyring plot (Figure 2B). We estimate a $\Delta H^{\ddagger}$ of 15.7 kcal/mol and a $\Delta S^{\ddagger}$ of −39.5 cal/mol·K for the barrier to CH_4 oxidation by $[CuOH]^+$. These are compared to values for CH_4 activation by $[Cu_2O]^{2+}$ in CHA in Table 1 where the MOR-A site is experimentally found to have a 9.5 kcal/mol higher enthalpic barrier.[14] This is a significant reactivity differential given that the range in $\Delta H^{\ddagger}$ between all identified

Table 1. Comparison of the Kinetic Parameters for the MOR-A $[CuOH]^+$ Site with Those of the Previously Studied $[Cu_2O]^{2+}$ Site in Cu-CHA

	$\Delta H^{\ddagger}$(kcal/mol)	$\Delta S^{\ddagger}$(kcal/mol)
$[CuOH]^+$	15.7	−39.5
$[Cu_2O]^{2+}$	6.2	−51.7

$[Cu_2O]^{2+}$ sites is less than 5 kcal/mol.[12−14] We now create an experimentally validated DFT model for the $[CuOH]^+$ active site and model the reactivity of this site in parallel with the $[Cu_2O]^{2+}$ site in CHA to better understand this large difference in the activation barrier for C−H abstraction from methane.

2.4. MOR-A Active Site Models. DFT models for the $[CuOH]^+$ site were constructed and compared to experimental data. MOR has four distinct T-sites (T1-4) with typically over 80% of the alumina concentrated at T1, T3, and T4,[34,35] which were then used to generate active site models (for visualization of the MOR T-sites, we direct readers to the following publications: refs 34 and 36). Each T-site has six edges where a $[CuOH]^+$ can bind bidentate to two oxygen atoms of the aluminate site. A $[CuOH]^+$ was placed at each of these locations for each T-site and optimized, generating 18 initial models (example structure in Figure 5). Due to steric constraints or the lack of a local minimum, some edges could not reasonably bind the $[CuOH]^+$, leaving the 11 models listed in Table S2. In all models, Cu binds bidentate to the anionic oxygen atoms of the aluminate T-site. The relative stability of each model was evaluated by calculating the binding energy for each $[CuOH]^+$. This was calculated as the energy of exchanging a Na^+ bound to the T-site for a bound $[CuOH]^+$ (eq 1) in the aqueous exchange step (modeled using a water polarizable continuum model).

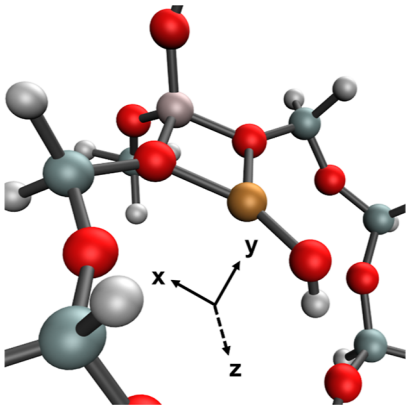


Figure 5. T1 Site 2 $[CuOH]^+$ active site model. (Color scheme: red = O, pink = Al, gray = Si, and mustard = Cu).

$$\text{binding energy} = E(Na^+ \text{ bound}) - E([CuOH]^+ \text{ bound}) \quad \text{(calculated relative between sites)} \qquad (1)$$

11 structures were obtained with stable geometries. The $[CuOH]^+$ binds to the lattice with a 15 kcal/mol range in energies across the various sites (Table S2). To probe the effect of second-sphere interactions on site stability, each model was truncated to just the $[CuOH]^+$, the bound aluminate, and the adjacent silica of the aluminate (example structure in Figure S19). The six most stable large models maintain the highest binding energies after truncation, indicating that the stability is predominantly related to the first coordination sphere. The most stable sites place the $[CuOH]^+$ close to the SiOAl planes of both O atoms and have narrower ∠SiOAl angles (<140° increasing p-character) to allow better bonding with the aluminate site. Note that all stable structures have a CuOH angle of 120−125° with the CuOH plane perpendicular to the *xy* plane formed by the T-site oxygen atoms, the Cu, and the oxygen of the hydroxide (Figure 5).

Time-dependent density functional theory (TD-DFT) and vibrational frequency calculations were performed on the 11 potential sites to compare with the experimental data (Table S2). The predicted most intense OH^- to Cu(II) CT transition energy ranges from 24 400 to 26 200 cm^{-1} and the Cu−OH stretch vibration ranges from 682−706 cm^{-1} across the 11 models; thus, the variability is small. The T1 Site 2 model in Figure 5 has a Cu−O stretch of 700 cm^{-1}, reasonably close to the 750 cm^{-1} vibration observed experimentally, while also having one of the highest binding energies. Thus, this was chosen as a reasonable active site model, but it is likely that the $[CuOH]^+$ binds in a range of stable locations with very similar spectral features.

An additional possible model was evaluated by adding a water ligand to the T1 Site 2 model. This four-coordinate model optimizes to a distorted square planar geometry (Figure S20) with a decrease in the Cu−O stretch to 600 cm^{-1} and a higher energy CT band at 27 000 cm^{-1}. Adding the water thus removes the low coordination environment necessary to form the strong Cu(II)−OH bond observed in rR spectroscopy, excluding this as a possible structure for MOR-A.

More in-depth spectroscopic analysis was performed on the T1 Site 2 $[CuOH]^+$ (Figure 5) model. The TD-DFT ligand field energies (Figure S21) match the bands observed in MCD (Figure 3). In addition to reproducing the Cu−O vibration, this T1 Site 2 model also reasonably predicts the low- and high-frequency rR peaks and their lack of isotope perturbations, as diagrammed in Figure 4B. The 552 cm^{-1} vibration is the symmetric lattice mode (also observed in the rR spectra of all $[Cu_2O]^{2+}$ sites)[12−14] and the 982 cm^{-1} vibration is a symmetric lattice bending mode where the Al T-Site Cu^{II}−OH site is predicted to distort along this mode upon OH^- to Cu(II) CT excitation (Explanation S3). We thus assign the MOR-A structure to a three-coordinate trigonal planar Cu(II) complex bound bidentate to the zeolite lattice with a strong

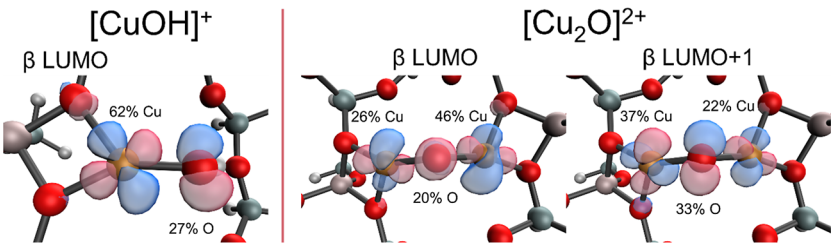


Figure 6. *β* LUMO of $[CuOH]^+$ (left) and *β* LUMO and *β* LUMO + 1 of $[Cu_2O]^{2+}$ (right). Mulliken orbital contributions given for each orbital. (Color scheme: red = O, pink = Al, gray = Si, and mustard = Cu).

extra-lattice OH^- ligand (Figure 5). The short Cu−OH bond in this model is a direct result of the O 2p-orbital (perpendicular to the O−H bond) in the xy plane π donating into the Cu(II) $d_{x^2-y^2}$ 1/2 occupied orbital. This results in the β lowest unoccupied molecular orbital (LUMO) in Figure 6 left, which is the frontier molecular orbital important for the reactivity, as explored below.

2.5. Reaction Coordinate Calculations: Comparison of $[CuOH]^+$ and $[Cu_2O]^{2+}$ Zeolite Active Sites. Having a well-defined mononuclear Cu(II) site and its experimental reactivity with CH_4, we can now evaluate why its activation barrier for this reaction is almost 10 kcal/mol higher experimentally than that of the binuclear $[Cu_2O]^{2+}$ site defined previously.[12−14] Second-sphere effects have been demonstrated to play a significant role in CH_4 activation in zeolites,[36] so larger models (83 atoms for $[CuOH]^+$ and 144 for $[Cu_2O]^{2+}$) that include the complete second-sphere around the active site were used to evaluate CH_4 reactivity (see Section S1.11). Unlike the $[Cu_2O]^{2+}$ site, which has two oxidizing equivalents to take methane fully to methanol, the $[CuOH]^+$ active site requires an additional site for methane oxidation. Snyder et al. demonstrated in the large pore *BEA iron zeolite that the methyl radical generated by HAA escapes the active site and reacts with a second active site.[37] In the case of $[CuOH]^+$ in large pore MOR, cage escape and reaction of a methyl radical with a second $[CuOH]^+$ site is necessary to fully generate methanol and would be consistent with the 0.33 ± 0.14 mol methanol/mol MOR-A produced (with some overoxidation). The sequential reactions of two $[CuOH]^+$ sites with methane and then the methyl radical generated in the first reaction were calculated using DFT (Figure 7A). The first $[CuOH]^+$ site performs HAA on CH_4, the resulting methyl radical migrates from hydrogen bonding to the $[CuOH_2]^+$ first product site into the large channel of MOR and subsequently reacts with a second $[CuOH]^+$ site. This generates two Cu(I) sites, a $[Cu(H_2O)]^+$ and a $[Cu(CH_3OH)]^+$, in an overall exothermic reaction (ΔH = −61.2 kcal/mol of CH_4). In this reaction coordinate, the barrier to HAA is 27.7 kcal/mol, while the barrier for migration of the methyl radical to exothermically react with the second $[CuOH]^+$ site is 8.4 (33 minus 24.6) kcal/mol.

The HAA reaction coordinate for the $[CuOH]^+$ site in MOR is compared to the previously calculated reaction coordinate for the $[Cu_2O]^{2+}$ site in CHA[14] in Figure 7B. The two sites have similar methane adsorption energies to the active site (9 ± 0.6 kcal/mol, Figure 7B far left to the reactant complex) and similar methyl radical adsorption energies to the H-atom abstracted first product sites (12.6 ± 0.1 kcal/mol, Figure 7B far right to product complexes), ruling out adsorption differences contributing to the barrier difference. However, in going from the reactant complex to the transition state, the $[CuOH]^+$ site has a calculated 10.8 kcal/mol higher energy barrier, about the same as the 9.5 kcal/mol barrier difference observed experimentally. Marcus theory was used to extract the intrinsic barrier, that is, the barrier with no thermodynamic driving force, using the method from Srnec and Solomon.[38] The intrinsic barriers for the $[CuOH]^+$ and $[Cu_2O]^{2+}$ sites are about the same (11.8 ± 0.6 kcal/mol) (Table 2). Thus, the difference in $\Delta H^{\ddagger}$ reflects the thermodynamic difference in the HAA reaction, a result of the difference in O−H bond strengths in the HAA products (Table 2 last column; determined from the extremes of Figure 7B relative to the calculated C−H bond strength of CH_4 with the same functional and basis set). The O−H bond strength of $[Cu_2OH]^{2+}$ is ∼15 kcal/mol higher than the O−H bond strength of $[CuOH_2]^+$. The origin of this difference is discussed below.

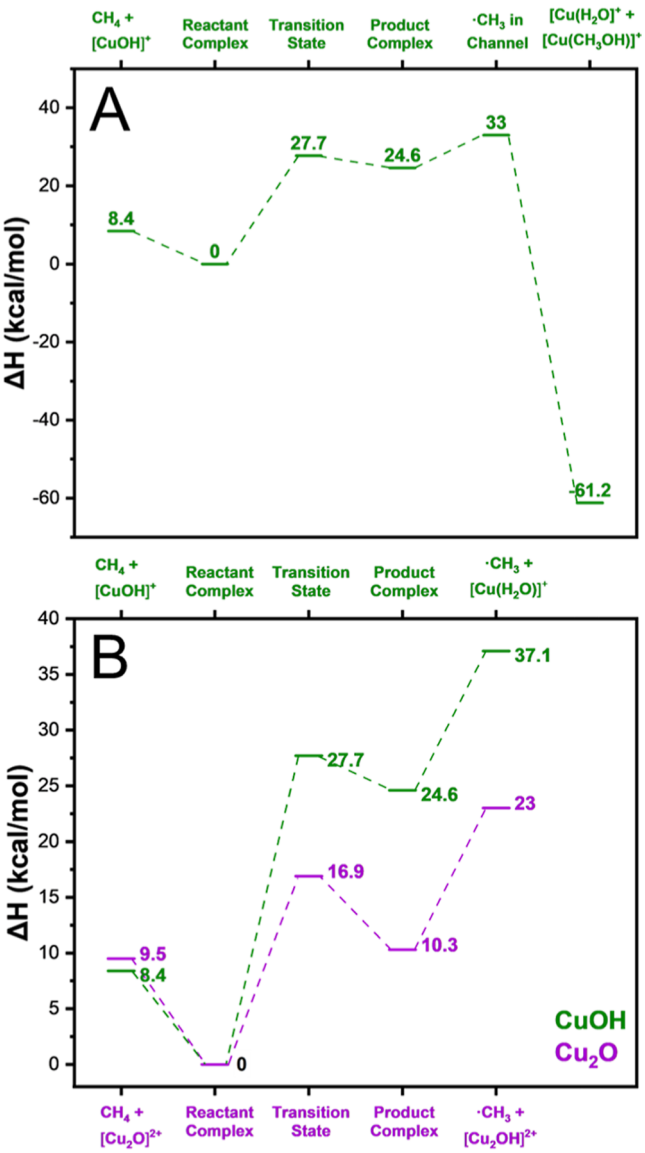


Figure 7. DFT-calculated HAA reaction coordinate. (A) Two $[CuOH]^+$ sites in MOR oxidizing methane to methanol with the methyl radical traveling through the zeolite channel between them. (B) Comparison between the $[CuOH]^+$ in MOR (green) and the $[Cu_2O]^{2+}$ in CHA (purple) with the final methyl radical in vacuum to compare adsorption effects. Reactant complex energies are set to zero.

Table 2. DFT-Calculated HAA Transition State Energies, Marcus Theory-Corrected Intrinsic Barriers, and Product OH Bond Strength (Calculated with Respect to the 103.3 kcal/mol Calculated C−H Bond Strength of CH_4) for $[CuOH]^+$ in MOR and $[Cu_2O]^{2+}$ in CHA

$\Delta H^{\ddagger}$(kcal/mol)	HAA TS	intrinsic barrier	product OH bond strength
$[CuOH]^+$	27.7	12.3	74.6
$[Cu_2O]^{2+}$	16.9	11.2	89.8

3. DISCUSSION

In past studies, autoreduced Cu-MOR was observed to produce methanol upon reaction with methane.[15,16] In this study, we combine EPR, XAS, DR UV−vis spectroscopy, MCD, and rR spectroscopy to define the active site for this reaction as a mononuclear $[CuOH]^+$ center bound bidentate to the zeolite lattice (Figure 5 and Table 3). This is distinct from the $[Cu_2O]^{2+}$ active site, which is reduced upon heating in helium to bicuprous sites that are reactivated by N_2O or O_2.[12−14]

Table 3. Summary of Spectroscopic Features and CH_4 Reactivity of the $[CuOH]^+$ (MOR-A) Active Site

	$[CuOH]^+$
g values	$g_\parallel = 2.27$, $g_\perp = 2.09$
A values (cm^{-1})	$A_\parallel = 191 \times 10^{-4}$, $A_\perp = 18.42 \times 10^{-4}$
Cu−O stretch (cm^{-1})	750
other rR vibrations (cm^{-1})	552, 981
OH^- to Cu(II) $dx^2 - y^2$ CT band (cm^{-1})	20 700
LF transactions (cm^{-1})	8900−16 500
$CH_4 \Delta H^\ddagger$(kcal/mol)	15.7
$CH_4 \Delta S^\ddagger$(cal/mol·K)	−39.5
percentage	30 ± 12%

We also identified this site in Cu-MFI with similar EPR parameters and a similar Cu−O stretch despite the very different topological structure of the MFI lattice. In both Cu-MOR and Cu-MFI, the $[CuOH]^+$ binds bidentate to a single T-site. However, this is not the case in all topologies. In LTA and FAU,[39] for example, no EPR parameters corresponding to the $[CuOH]^+$ site assigned here are observed. We speculate that in lattices with an adjacent aluminate and silicate T-site positioned to bind the copper tridentate, different mononuclear Cu^{II} sites could form with different spectroscopic handles.

Additionally, because of the ability to selectively reduce the $[Cu_2O]^{2+}$ site through heating in helium, we are able to isolate the single $[CuOH]^+$ site as the sole source of methanol production in autoreduced Cu-MOR. This contrasts with the N_2O-activated zeolite, which still has the $[CuOH]^+$ site but also has $[Cu_2O]^{2+}$ active sites. This is also true in N_2O activated Cu-MFI (Figures S15-S17).[12] This suggests that analyzing autoreduced Cu zeolites, in addition to the activated materials, is important in elucidating active site contributions to reactivity. This also provides further support for the use of site-selective techniques such as rR spectroscopy and high-resolution techniques such as EPR for analyzing active sites in Cu zeolites. In the case of N_2O-activated Cu-MOR and Cu-MFI, bulk techniques such as extended X-ray absorption fine structure contain signals from multiple Cu sites simultaneously and limit the ability to parse for relevant information.

Although this $[CuOH]^+$ site has been invoked multiple times in the literature, there have been competing proposals of reactivity.[19,20] We find that the $[CuOH]^+$ site has a 10 kcal/mol higher barrier for HAA from CH_4 than the comparably well-defined $[Cu_2O]^{2+}$ site. Through computational modeling, we find that these two sites have similar intrinsic barriers. This is a result of the similarly high covalency of their frontier molecular orbitals: $[CuOH]^+$ (27% O character in the β LUMO) and $[Cu_2O]^{2+}$ (20% O character in the β LUMO and 33% O character in the β LUMO + 1) (Figure 6). This allows a strong orbital overlap with the H−C bond of CH_4 for HAA. The low coordination number enforced by the Al T-sites of the zeolite lattice results in strong hydroxo and oxo ligand to Cu(II) π-donor bonds for both motifs. This is amplified by the relatively weak donation by the zeolite Al T-site bidentate ligation. In the case of the mononuclear MOR-A site studied here, the strong Cu−OH π bond is revealed by its high energy Cu−O stretch and its low-energy ligand to metal CT transition.

Thus, given the similar intrinsic barriers, the difference in $\Delta H^\ddagger$ reflects the thermodynamic difference in the HAA reaction, a result of the difference in O−H bond strengths in the $[CuOH_2]^+$ and $[Cu_2OH]^{2+}$ first products. To understand the origin of the O−H bond strength difference, the H-atom transfer was separated into reduction and protonation steps (Figure S22). The $[Cu_2O]^{2+}$ site is 16 kcal/mol easier to reduce than the $[CuOH]^+$ site, about equal to the enthalpy difference calculated for the addition of the H-atom to each site by HAA. The resulting reduced $[Cu_2O]^+$ and $[CuOH]^+$ sites have roughly the same proton affinities due in part to both having a Mulliken charge of −0.9 ± 0.05 on the extra-lattice oxygen ligand. Thus, the thermodynamic difference in the reaction reflects the greater electron affinity of the oxo-bridged binuclear site than that of the mononuclear $[CuOH]^+$ site.

This higher affinity in the binuclear site appears to correlate with the delocalization of the added electron from HAA over the two Cu centers as the unpaired electron is equally shared over both copper ions (Figure S23C). To evaluate the impact of this delocalization on the electron affinity, a model $[CuOZn]^{2+}$ zeolite site was generated by replacing one of the Cu atoms in the $[Cu_2O]^{2+}$ site with a closed shell d^{10} Zn^{2+}. This leaves the single d^9 Cu^{2+} to accept the electron and localizes the added electron only on one metal in the reduced structure. The electron affinity of this model is compared to the mononuclear and binuclear Cu structures below

$$\begin{aligned} [Cu_2O]^{2+} + e^- &\rightarrow [Cu_2O]^+ \quad \Delta\Delta H = 0 \text{ (defined)} \\ [CuOH]^+ + e^- &\rightarrow [CuOH] \quad \Delta\Delta H = 16 \text{ kcal/mol} \\ [CuOZn]^{2+} + e^- &\rightarrow [CuOZn]^+ \quad \Delta\Delta H = 20 \text{ kcal/mol} \end{aligned} \tag{2}$$

Localizing the electron in the binuclear structure lowers the electron affinity by 20 kcal/mol relative to $[Cu_2O]^{2+}$. The $[CuOH]^+$ site is actually easier to reduce than the $[CuOZn]^{2+}$ structure due to the greater antibonding character of the oxo-Cu bridge (Figure S24) and electronic relaxation effects (geometric relaxation has a negligible effect). This indicates that delocalization of the electron over the two $Cu^{1.5}$ ions substantially increases the electron affinity of the $[Cu_2O]^{2+}$ site.

To quantify this delocalization contribution to the electron affinity in $[Cu_2O]^{2+}$, the Piepho, Krausz, and Schatz (PKS) theory for the potential energy surfaces of mixed valence sites was applied.[40,41] In the PKS theory, mixed-valent structures have competing stabilizing contributions. The electronic coupling between the two metal ions (H_{ab}) creates stabilization through delocalization of the unpaired electron, favoring a totally symmetric structure with half integer oxidation states. This is opposed by vibronic trapping (λ), which lowers the energy as the structure becomes asymmetric to trap the electron on one metal. Here, one metal's bonds contract and the others' bonds expand, localizing the electron on the metal

with longer bonds. These competing contributions were evaluated using DFT calculations to map the potential energy surface along a vibrational mode where the structure distorts from a symmetric delocalized structure to the asymmetric localized structure. This Q_ vibrational mode was created by optimizing the one electron reduced $[CuOZn]^+$ structure where the additional electron is localized on the Cu and subsequently replacing the Zn(II) with Cu(II) without optimization. This creates the $[Cu_2O]^+$ asymmetric structural limit in this vibration. To complete the vibrational mode, the change in atomic positions from the delocalized structure to the localized structure was used to create points of varying distortion (example structures in Figure S25). The DFT-calculated energies of the points along this vibration are given by the solid squares in Figure 8. The DFT-calculated potential

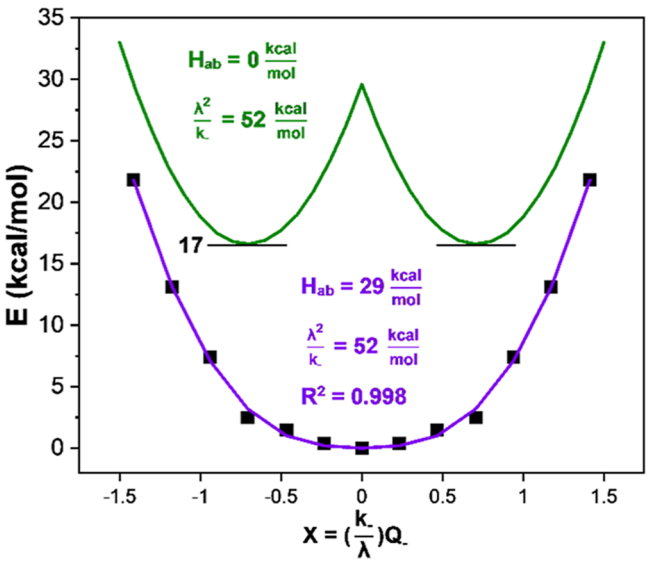


Figure 8. DFT-calculated change in energy of $[Cu_2O]^+$ upon distortion along the Q_ mode (black squares). Fit of black squares to eq 3 (purple). Plot of the potential energy surface with parameters from the fit with H_{ab} set to zero to simulate the localized structure (green).

energy surface was then fit with a potential energy equation that includes the electronic coupling associated with the electron delocalization (H_{ab}) and vibronic trapping that localizes the electron on one center (λ), where k- is the vibrational force constant in the Q_ mode and $x = \left(\frac{k_-}{\lambda}\right)Q_-$ (eq 3).

$$E = \frac{1}{2}\left(\frac{\lambda^2}{k_-}\right)x^2 - \sqrt{\frac{1}{2}\left(\frac{\lambda^2}{k_-}\right)^2 x^2 + H_{ab}^2} \quad (3)$$

From the purple fit in Figure 8, the derived H_{ab} term is 29 kcal/mol, which overcomes the vibronic trapping, resulting in the minimum at the symmetric delocalized structure. To estimate the effect of the delocalization on the total energy, the H_{ab} term was then set to zero, and the potential energy surfaces were re-plotted to simulate the localized structures (Figure 8 green). This surface contains two local minima resulting from vibronic trapping of the extra e^- on either Cu with energies at +17 kcal/mol. Thus, the electron delocalization stabilizes the HAA first product by 17 kcal/mol, and without this delocalization, the electron affinity of the $[Cu_2O]^{2+}$ site would actually be lower than that of the $[CuOH]^+$ site by 1 kcal/mol (eq 2).

This electron delocalization is a direct result of the superexchange interaction between the two copper ions through the bridging oxo ligand. As seen in Figure 9 (extracted

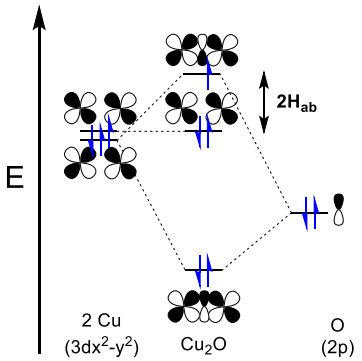


Figure 9. Molecular orbital diagram for the bonding interaction of 2 Cu $3dx^2 - y^2$ orbitals with the bridging oxo 2p-orbital. The highest energy orbital is 1/2 occupied, while the lower energy orbitals are fully occupied.

from DFT contours given in Figure S23), the $3d_{x^2-y^2}$ orbitals on the two Cu ions form symmetric and antisymmetric combinations. The symmetric combination undergoes a π bonding/antibonding interaction with the bridging oxo 2p-orbital (bottom and top molecular orbitals), while the antisymmetric combination remains non-bonding (middle orbital). The energy of excitation from the non-bonding orbital (middle) to the antibonding symmetric β LUMO (top) is equal to 2 H_{ab}. TD-DFT calculations predict this transition at 18 400 cm^{-1}, giving an H_{ab} of 27 kcal/mol, in reasonable agreement with the value obtained from mapping the potential energy surface in Figure 8 (29 kcal/mol). Thus, the strong π donor oxo bridge facilitates the electronic interaction between the copper ions, delocalizes the added electron gained from the reaction with CH_4, lowers the reaction barrier, and enables low-temperature methane oxidation. Four $[Cu_2O]^{2+}$ sites have been rigorously defined so far.[10,12,13,36] For all of these sites, the DFT models of the HAA $[Cu_2OH]^{2+}$ product have significant delocalization of the added electron across both copper centers (Table S3). Thus, product electron delocalization appears to be a general driving force in this active site motif.

4. CONCLUSIONS

Electronic coupling between metals in mixed-valent systems has enabled rapid electron transfer in bioinorganic chemistry, the synthesis of new molecular electronics, and other important chemical phenomena.[42−44] Here, we illuminate a new application of mixed-valent metal chemistry: improving methane oxidation and catalysis. To make copper-containing zeolites industrially viable for methane oxidation, a high density of low-temperature reactive active sites is necessary. Although there have been conflicting reports in the literature on the reactivity of a mononuclear $[CuOH]^+$ site, here, we elucidate that the site is clearly less reactive than the binuclear $[Cu_2O]^{2+}$ site. Thus, better zeolite design should concentrate on forming bridged multinuclear copper species rather than monomeric sites. We also suggest that a bridged multinuclear Cu site would potentially allow the low-temperature reactivity

of pMMO by delocalizing the electron gained from HAA and driving the reaction. This delocalization principle also applies to the design of industrial catalysts generally. New active sites in redox catalysis could benefit from increased metal nuclearity with a strong bridging ligand, facilitating electronic coupling, allowing electron delocalization, and ultimately enabling low-temperature reactivity.

■ ASSOCIATED CONTENT

Supporting Information

The Supporting Information is available free of charge at https://pubs.acs.org/doi/10.1021/jacs.2c06269.

Experimental section, PXRD patterns, nitrogen sorption isotherms, rR profile, XAS fits, linear coupling term calculations, DFT cluster model coordinates, DR UV–vis spectra, EPR spectra, MCD spectra, decay of the $[CuOH]^+$ CT band and the first-order plot of the decay, truncated structure of T1 site 2 $[CuOH]^+$, DFT calculated energetics of addition of a hydrogen atom to the active sites, orbital contours and contributions, and extended X-ray absorption fine structure spectra (PDF)

■ AUTHOR INFORMATION

Corresponding Authors

Robert A. Schoonheydt − *Department of Microbial and Molecular Systems, Center for Sustainable Catalysis and Engineering, KU Leuven-University of Leuven, Leuven B-3001, Belgium*; Email: robert.schoonheydt@kuleuven.be

Bert F. Sels − *Department of Microbial and Molecular Systems, Center for Sustainable Catalysis and Engineering, KU Leuven-University of Leuven, Leuven B-3001, Belgium*; orcid.org/0000-0001-9657-1710; Email: bert.sels@kuleuven.be

Edward I. Solomon − *Department of Chemistry, Stanford University, Stanford, California 94305, United States; Stanford Synchrotron Radiation Lightsource, SLAC National Accelerator Laboratory, Menlo Park, California 94025, United States*; orcid.org/0000-0003-0291-3199; Email: edward.solomon@stanford.edu

Authors

Alexander J. Heyer − *Department of Chemistry, Stanford University, Stanford, California 94305, United States*; orcid.org/0000-0003-4362-8191

Dieter Plessers − *Department of Microbial and Molecular Systems, Center for Sustainable Catalysis and Engineering, KU Leuven-University of Leuven, Leuven B-3001, Belgium*

Augustin Braun − *Department of Chemistry, Stanford University, Stanford, California 94305, United States*; orcid.org/0000-0002-9487-5769

Hannah M. Rhoda − *Department of Chemistry, Stanford University, Stanford, California 94305, United States*; orcid.org/0000-0001-5730-5209

Max L. Bols − *Department of Microbial and Molecular Systems, Center for Sustainable Catalysis and Engineering, KU Leuven-University of Leuven, Leuven B-3001, Belgium*; orcid.org/0000-0002-4576-5969

Britt Hedman − *Stanford Synchrotron Radiation Lightsource, SLAC National Accelerator Laboratory, Menlo Park, California 94025, United States*

Keith O. Hodgson − *Department of Chemistry, Stanford University, Stanford, California 94305, United States; Stanford Synchrotron Radiation Lightsource, SLAC National Accelerator Laboratory, Menlo Park, California 94025, United States*

Complete contact information is available at: https://pubs.acs.org/10.1021/jacs.2c06269

Author Contributions

[‖]A.J.H. and D.P. contributed equally to this work.

Notes

The authors declare no competing financial interest.

■ ACKNOWLEDGMENTS

Funding for this work was provided by the Stanford Woods Institute for the Environment grant SPO 164153 WTAQE (to E.I.S.), the Stanford Natural Gas Initiative grant SPO 127222 WZABN (to E.I.S.), the National Institutes of Health Grant R01DK031450 (to E.I.S.), the Anne T. and Robert M. Bass Stanford Graduate Fellowship (to A.J.H.), and the Research Foundation—Flanders is acknowledged for grants G0A0321N (to D.P. and B.F.S.) and 1276021N (to M.B.). We thank Matthew Latimer, Leah Kelly, Ritimukta Sarangi, and Macon Abernathy for assistance with XAS experiments at SSRL. The use of the Stanford Synchrotron Radiation Lightsource, SLAC National Accelerator Laboratory, is supported by the US Department of Energy (DOE), Office of Science, Office of Basic Energy Sciences under Contract DE-AC02-76SF00515. The SSRL Structural Molecular Biology Program is supported by the DOE Office of Biological and Environmental Research and by the National Institutes of Health, National Institute of General Medical Sciences (grant P41GM103393 to K.O.H. and B.H.). The contents of this publication are solely the responsibility of the authors and do not necessarily represent the official views of NIGMS or NIH. Some of the computing for this project was performed on the Sherlock cluster. We would like to thank Stanford University and the Stanford Research Computing Center for providing computational resources and support that contributed to these research results.

■ REFERENCES

(1) Tang, P.; Zhu, Q.; Wu, Z.; Ma, D. Methane Activation: The Past and Future. *Energy Environ. Sci.* **2014**, *7*, 2580–2591.

(2) Jacobs, A. B.; Banerjee, R.; Deweese, D. E.; Braun, A.; Babicz, J. T.; Gee, L. B.; Sutherlin, K. D.; Böttger, L. H.; Yoda, Y.; Saito, M.; Kitao, S.; Kobayashi, Y.; Seto, M.; Tamasaku, K.; Lipscomb, J. D.; Park, K.; Solomon, E. I. Nuclear Resonance Vibrational Spectroscopic Definition of the Fe(IV)2 Intermediate Q in Methane Monooxygenase and Its Reactivity. *J. Am. Chem. Soc.* **2021**, *143*, 16007–16029.

(3) Schulz, C. E.; Castillo, R. G.; Pantazis, D. A.; DeBeer, S.; Neese, F. Structure-Spectroscopy Correlations for Intermediate Q of Soluble Methane Monooxygenase: Insights from QM/MM Calculations. *J. Am. Chem. Soc.* **2021**, *143*, 6560–6577.

(4) Ross, M. O.; Rosenzweig, A. C. A Tale of Two Methane Monooxygenases. *J. Biol. Inorg Chem.* **2017**, *22*, 307–319.

(5) Chan, S. I.; Wang, V. C. C.; Lai, J. C. H.; Yu, S. S. F.; Chen, P. P. Y.; Chen, K. H. C.; Chen, C. L.; Chan, M. K. Redox Potentiometry Studies of Particulate Methane Monooxygenase: Support for a Trinuclear Copper Cluster Active Site. *Angew. Chem., Int. Ed.* **2007**, *46*, 1992–1994.

(6) Chang, W. H.; Lin, H. H.; Tsai, I. K.; Huang, S. H.; Chung, S. C.; Tu, I. P.; Yu, S. S. F.; Chan, S. I. Copper Centers in the Cryo-EM

Structure of Particulate Methane Monooxygenase Reveal the Catalytic Machinery of Methane Oxidation. *J. Am. Chem. Soc.* **2021**, *143*, 9922−9932.
(7) Ross, M. O.; MacMillan, F.; Wang, J.; Nisthal, A.; Lawton, T. J.; Olafson, B. D.; Mayo, S. L.; Rosenzweig, A. C.; Hoffman, B. M. Particulate Methane Monooxygenase Contains Only Mononuclear Copper Centers. *Science* **2019**, *364*, 566−570.
(8) Koo, C. W.; Tucci, F. J.; He, Y.; Rosenzweig, A. C. Recovery of Particulate Methane Monooxygenase Structure and Activity in a Lipid Bilayer. *Science* **2022**, *375*, 1287−1291.
(9) Snyder, B. E. R.; Bols, M. L.; Schoonheydt, R. A.; Sels, B. F.; Solomon, E. I. Iron and Copper Active Sites in Zeolites and Their Correlation to Metalloenzymes. *Chem. Rev.* **2018**, *118*, 2718−2768.
(10) Rhoda, H. M.; Heyer, A. J.; Snyder, B. E. R.; Plessers, D.; Bols, M. L.; Schoonheydt, R. A.; Sels, B. F.; Solomon, E. I. Second-Sphere Lattice Effects in Copper and Iron Zeolite Catalysis. *Chem. Rev.* **2022**, *122*, 12207−12243.
(11) Newton, M. A.; Knorpp, A. J.; Sushkevich, V. L.; Palagin, D.; van Bokhoven, J. A. Active Sites and Mechanisms in the Direct Conversion of Methane to Methanol Using Cu in Zeolitic Hosts: A Critical Examination. *Chem. Soc. Rev.* **2020**, *49*, 1449−1486.
(12) Woertink, J. S.; Smeets, P. J.; Groothaert, M. H.; Vance, M. A.; Sels, B. F.; Schoonheydt, R. A.; Solomon, E. I. A [Cu 2 O] 2+ core in Cu-ZSM-5, the active site in the oxidation of methane to methanol. *Proc. Natl. Acad. Sci. U.S.A.* **2009**, *106*, 18908−18913.
(13) Vanelderen, P.; Snyder, B. E. R.; Tsai, M. L.; Hadt, R. G.; Vancauwenbergh, J.; Coussens, O.; Schoonheydt, R. A.; Sels, B. F.; Solomon, E. I. Spectroscopic Definition of the Copper Active Sites in Mordenite: Selective Methane Oxidation. *J. Am. Chem. Soc.* **2015**, *137*, 6383−6392.
(14) Rhoda, H. M.; Plessers, D.; Heyer, A. J.; Bols, M. L.; Schoonheydt, R. A.; Sels, B. F.; Solomon, E. I. Spectroscopic Definition of a Highly Reactive Site in Cu-CHA for Selective Methane Oxidation: Tuning a Mono-μ-Oxo Dicopper(II) Active Site for Reactivity. *J. Am. Chem. Soc.* **2021**, *143*, 7531−7540.
(15) Sushkevich, V. L.; Palagin, D.; Ranocchiari, M.; Van Bokhoven, J. A. Selective Anaerobic Oxidation of Methane Enables Direct Synthesis of Methanol. *Science* **2017**, *356*, 523−527.
(16) Brezicki, G.; Kammert, J. D.; Gunnoe, T. B.; Paolucci, C.; Davis, R. J. Insights into the Speciation of Cu in the Cu-H-Mordenite Catalyst for the Oxidation of Methane to Methanol. *ACS Catal.* **2019**, *9*, 5308−5319.
(17) Kulkarni, A. R.; Zhao, Z. J.; Siahrostami, S.; Nørskov, J. K.; Studt, F. Monocopper Active Site for Partial Methane Oxidation in Cu-Exchanged 8MR Zeolites. *ACS Catal.* **2016**, *6*, 6531−6536.
(18) Oord, R.; Schmidt, J. E.; Weckhuysen, B. M. Methane-to-Methanol Conversion over Zeolite Cu-SSZ-13, and Its Comparison with the Selective Catalytic Reduction of NOx with NH3. *Catal. Sci. Technol.* **2018**, *8*, 1028−1038.
(19) Sushkevich, V. L.; Artsiusheuski, M.; Klose, D.; Jeschke, G.; Bokhoven, J. A. Identification of Kinetic and Spectroscopic Signatures of Copper Sites for Direct Oxidation of Methane to Methanol. *Angew. Chem., Int. Ed.* **2021**, *60*, 15944−15953.
(20) Pappas, D. K.; Borfecchia, E.; Dyballa, M.; Pankin, I. A.; Lomachenko, K. A.; Martini, A.; Signorile, M.; Teketel, S.; Arstad, B.; Berlier, G.; Lamberti, C.; Bordiga, S.; Olsbye, U.; Lillerud, K. P.; Svelle, S.; Beato, P. Methane to Methanol: Structure-Activity Relationships for Cu-CHA. *J. Am. Chem. Soc.* **2017**, *139*, 14961−14975.
(21) Tomkins, P.; Mansouri, A.; Bozbag, S. E.; Krumeich, F.; Park, M. B.; Alayon, E. M. C.; Ranocchiari, M.; van Bokhoven, J. A. Isothermal Cyclic Conversion of Methane into Methanol over Copper-Exchanged Zeolite at Low Temperature. *Angew. Chem.* **2016**, *128*, 5557−5561.
(22) Kucherov, A. V.; Slinkin, A. A.; Kondrat'ev, D. A.; Bondarenko, T. N.; Rubinstein, A. M.; Minachev, K. M. Cu2+-cation location and reactivity in mordenite and ZSM-5: e.s.r.-study. *Zeolites* **1985**, *5*, 320−324.
(23) Vanelderen, P.; Vancauwenbergh, J.; Tsai, M. L.; Hadt, R. G.; Solomon, E. I.; Schoonheydt, R. A.; Sels, B. F. Spectroscopy and Redox Chemistry of Copper in Mordenite. *ChemPhysChem* **2014**, *15*, 91−99.
(24) Oliva, C.; Selli, E.; Ponti, A.; Correale, L.; Solinas, V.; Rombi, E.; Monaci, R.; Forni, L. FTIR and EPR Characterisation of Copper-Exchanged Mordenites and Beta Zeolites. *J. Chem. Soc. Faraday. Trans.* **1997**, *93*, 2603−2608.
(25) Kau, L.-S.; Spira-Solomon, D. J.; Penner-Hahn, J. E.; Hodgson, K. O.; Solomon, E. I. X-ray absorption edge determination of the oxidation state and coordination number of copper. Application to the type 3 site in Rhus vernicifera laccase and its reaction with oxygen. *J. Am. Chem. Soc.* **1987**, *109*, 6433−6442.
(26) Mason, W. R.*A Practical Guide to Magnetic Circular Dichroism Spectroscopy*; John Wiley & Sons, Inc.: Hoboken, New Jersey, 2007.
(27) Pugh, S. M.; Wright, P. A.; Law, D. J.; Thompson, N.; Ashbrook, S. E. Facile, Room-Temperature 17O Enrichment of Zeolite Frameworks Revealed by Solid-State NMR Spectroscopy. *J. Am. Chem. Soc.* **2020**, *142*, 900−906.
(28) Spaeth, A. D.; Gagnon, N. L.; Dhar, D.; Yee, G. M.; Tolman, W. B. Determination of the Cu(III)-OH Bond Distance by Resonance Raman Spectroscopy Using a Normalized Version of Badger's Rule. *J. Am. Chem. Soc.* **2017**, *139*, 4477−4485.
(29) Grundner, S.; Markovits, M. A. C.; Li, G.; Tromp, M.; Pidko, E. A.; Hensen, E. J. M.; Jentys, A.; Sanchez-Sanchez, M.; Lercher, J. A. Single-Site Trinuclear Copper Oxygen Clusters in Mordenite for Selective Conversion of Methane to Methanol. *Nat. Commun.* **2015**, *6*, 1−9.
(30) Lee, S. K.; George, S. D. B.; Antholine, W. E.; Hedman, B.; Hodgson, K. O.; Solomon, E. I. Nature of the Intermediate Formed in the Reduction of O2 to H2O at the Trinuclear Copper Cluster Active Site in Native Laccase. *J. Am. Chem. Soc.* **2002**, *124*, 6180−6193.
(31) Woertink, J. S.; Tian, L.; Maiti, D.; Lucas, H. R.; Himes, R. A.; Karlin, K. D.; Neese, F.; Würtele, W.; Holthausen, M. C.; Bill, X. E.; Sundermeyer, S.; Schindler, E. I.; Solomon, E. I. Spectroscopic and Computational Studies of an End-on Bound Superoxo-Cu(II) Complex: Geometric and Electronic Factors That Determine the Ground State. *Inorg. Chem.* **2010**, *49*, 9450−9459.
(32) Crespo, A.; Martı, M. A.; Roitberg, A. E.; Amzel, L. M. The Catalytic Mechanism of Peptidylglycine r -Hydroxylating Monooxygenase Investigated by Computer Simulation. *J. Am. Chem. Soc.* **2006**, *128*, 12817−12828.
(33) Chen, P.; Fujisawa, K.; Solomon, E. I. Spectroscopic and Theoretical Studies of Mononuclear Copper(II) Alkyl- and Hydroperoxo Complexes: Electronic Structure Contributions to Reactivity. *J. Am. Chem. Soc.* **2000**, *122*, 10177−10193.
(34) Alberti, A. Location of Brønsted Sites in Mordenite. *Zeolites* **1997**, *19*, 411−415.
(35) Dědeček, J.; Sobalík, Z.; Wichterlová, B. Siting and Distribution of Framework Aluminium Atoms in Silicon-Rich Zeolites and Impact on Catalysis. *Catal. Rev.* **2012**, *54*, 135−223.
(36) Snyder, B. E. R.; Vanelderen, P.; Schoonheydt, R. A.; Sels, B. F.; Solomon, E. I. Second-Sphere Effects on Methane Hydroxylation in Cu-Zeolites. *J. Am. Chem. Soc.* **2018**, *140*, 9236−9243.
(37) Snyder, B. E. R.; Bols, M. L.; Rhoda, H. M.; Plessers, D.; Schoonheydt, R. A.; Sels, B. F.; Solomon, E. I. Cage Effects Control the Mechanism of Methane Hydroxylation in Zeolites. *Science* **2021**, *373*, 327−331.
(38) Srnec, M.; Solomon, E. I. Frontier Molecular Orbital Contributions to Chlorination versus Hydroxylation Selectivity in the Non-Heme Iron Halogenase SyrB2. *J. Am. Chem. Soc.* **2017**, *139*, 2396−2407.
(39) Schoonheydt, R. A. Transition Metal Ions in Zeolites: Siting and Energetics of Cu2+. *Catal. Rev.* **1993**, *35*, 129−168.
(40) Piepho, S. B.; Krausz, E. R.; Schatz, P. N. Vibronic Coupling Model for Calculation of Mixed Valence Absorption Profiles. *J. Am. Chem. Soc.* **1978**, *100*, 2996−3005.

(41) Schatz, P. N.Mixed Valence. In *Inorganic Electronic Structure and Spectroscopy. Volume II Applications and Case Studies*; Solomon, E. I., Lever, A. B. P., Eds.; Wiley, 1999; pp 175−226.
(42) Richardson, D. E.; Taube, H. Mixed-Valence Molecules: Electronic Delocalization and Stabilization. *Coord. Chem. Rev.* **1984**, *60*, 107−129.
(43) Solomon, E. I.; Xie, X.; Dey, A. Mixed Valent Sites in Biological Electron Transfer. *Chem. Soc. Rev.* **2008**, *37*, 623−638.
(44) Launay, J. P. Mixed-Valent Compounds and their Properties - Recent Developments. *Eur. J. Inorg. Chem.* **2020**, *2020*, 329−341.